ROYAL SOCIETY OF CHEMISTRY

PAPER

Check for updates

A single-crystal nickel-rich material as a highly stable cathode for lithium-ion batteries†

Aihua Ran,[ab] Shuxiao Chen,[ab] Ming Cheng,[ab] Zheng Liang,[ab] Baohua Li, [ID][b] Guangmin Zhou, [ID] *[ab] Feiyu Kang,[ab] Xuan Zhang*[ab] and Guodan Wei [ID] *[ab]

The commonly used polycrystalline Ni-rich LiNi$_{0.8}$Co$_{0.1}$Mn$_{0.1}$O$_2$ (NCM811) cathode materials suffer from electrochemical degradation such as rapid impedance growth and capacity decay due to their intrinsically vulnerable grain-boundary fracture during battery cycling. To understand the effect of the aging mechanism of the nanocrystalline grains on the cycling performance, we have investigated polycrystalline (P-NCM811) and single-crystal (S-NCM811) nanoscale cathode materials and compared their impact on the battery performance. Interestingly, the capacity retention of the S-NCM 811 cathode has faded slowly after 200 cycles at 1C rate with a capacity retention of 80%, compared to the P-NCM 811 cathode with a value of 72%. *In situ* X-ray diffraction and *ex situ* scanning electron microscopy analyses reveal that the irreversible structural and phase changes have impacted the performance of P-NCM811, especially under varied temperature conditions. The surface side reaction and internal crystal domains that generate structural defects were found to impair the diffusion of lithium ions and, eventually, lead to rapid capacity fading and poor cycling stability. These results give guidance on further developments in the particle morphology to dissipate the intrinsic lattice strain, stabilize the surface, and modify the composition to finally attain a satisfactory cycling stability.

1. Introduction

Lithium-ion batteries (LIBs) are broadly utilized power sources in portable electronics, electric vehicles (EVs) and energy storage systems (EESs), due to their scalability, reliability, and adaptability.[1] However, it is still a challenge to achieve the high energy density target by only using LiFePO$_4$,[2] LiNi$_{1/3}$Co$_{1/3}$Mn$_{1/3}$O$_2$(ref. 3) or LiMn$_2$O$_4$(ref. 4) as a cathode and commercial graphite as an anode. Exhilaratingly, the combination of Ni-rich LiNi$_x$Co$_y$Mn$_{1-x-y}$O$_2$ cathodes (Ni-rich NCM, $x \geq 0.6$) with high-capacity silicon-carbon anodes can effectively enable high energy density.[5,6] The Ni-rich NCM positive active material has high specific energy, high power, and long cycle life, and is becoming the primary choice for the next generation of LIBs.[7] It is well known that a higher specific capacity can be reached as the nickel content increases within the NCM system. However, the practical application is constrained by the structural instability,[8] low capacity retention,[9] poor thermal stability,[10] and insufficient safety. Consequently, understanding the aging mechanisms including irreversible structural collapse, surface

[a]Tsinghua-Berkeley Shenzhen Institute (TBSI), Tsinghua University, Shenzhen, 518055, China. E-mail: guangminzhou@sz.tsinghua.edu.cn; xuanzhang@sz.tsinghua.edu.cn; weiguodan@sz.tsinghua.edu.cn

[b]Tsinghua Shenzhen International Graduate School, Tsinghua University, Shenzhen, 518055, China

† Electronic supplementary information (ESI) available. See DOI: 10.1039/d2ta01186g

side reactions, and internal crystal domains is necessary to further develop and utilize Ni-rich cathode materials.

Conventionally, in LIBs with intercalation-based cathode active materials, the reversible capacity of the cell is limited by the initial concentration of lithium ions stored in the cathode. Under ideal cycling conditions, Li$^+$ ions are transported between the cathode and anode, without any irrecoverable loss. Under practical conditions, side reactions taking place during normal operation gradually diminish the amount of lithium that can be shuttled between the cathode and anode.[3,11] For example, when the Ni-rich cathode materials are exposed to moist air, they promptly react with H$_2$O and CO$_2$ to form LiOH, LiHCO$_3$, and Li$_2$CO$_3$ coated on the particle surface.[12,13] Meanwhile, the unstable Ni^{3+} would spontaneously transform into Ni^{2+}, generating active oxygen species.[14] Additionally, a NiO rock-salt structure is formed on the surface with the consumption of Li$^+$ and the release of lattice oxygen.[15,16] The mechanical stress induced by anisotropic volume change indeed causes microcracking and eventual disintegration of the Ni-rich NCM particles by inter-granular breakage.[17] To reduce these side reactions, researchers have devoted a lot of effort towards modification, such as bulk doping,[18] surface coating,[19,20] and developing new electrolyte systems[21] to improve Ni-rich NCM cathodes.

Among the ternary Ni-rich materials, polycrystalline LiNi$_{0.8}$Co$_{0.1}$Mn$_{0.1}$O$_2$ (P-NCM811) has attracted much attention as the cathode material, which could be attributed to the outstanding

19680 | *J. Mater. Chem. A*, 2022, **10**, 19680–19689

This journal is © The Royal Society of Chemistry 2022

electrochemical performance and excellent thermal stability at the fully charged state.[22,23] Unfortunately, P-NCM811 materials still suffered from some major drawbacks, which hindered their utilization in LIBs, such as a low initial coulombic efficiency in the first charge/discharge process, an undesirable rate capability, and poor cycling stability.[20] The breakage of polycrystalline particles and electrolyte infiltration can lead to side effects and rapid capacity decay, limiting their application.[24,25] In addition, when ternary LIBs are working, there will be temperature accumulation inside the battery.[26,27] According to previous reports,[28] the internal temperature hardly exceeds 300 °C (if the temperature is too high, the battery will fail before reaching such a temperature).[29] In Ni-rich NCM compositions, thermal stability, which is crucial for avoiding catastrophic failures, as well as cycle stability drastically dropped as the nickel content increases within the NCM system.[10,30] A significant improvement in capacity retention was reported with "single-crystalline" NCM (S-NCM).[27,31] The monolithic microstructure of this new type of cathode material together with coating and suitable electrolyte additives successfully reduced the impact of parasitic processes and secondary particle cracking, significantly increasing the rate, cycling performance and thermal stability.[32] At present, many studies mainly focus on improving the cycling stability of P-NCM, whereas less attention has been paid to examine the root causes and main influencing factors of the electrochemical performance differences between P-NCM and S-NCM.

Herein, the aging mechanisms and thermal stability of P-NCM811 and S-NCM811 are considered and compared. We heated two samples to different temperatures to see the morphology change and structural stability through *ex situ* scanning electron microscopy (SEM). Moreover, *in situ* X-ray diffraction (XRD) was used to observe the phase transformation and irreversible change of Ni-rich single crystal and polycrystalline materials after different heat treatments. In addition, cyclic voltammetry (CV) results show that there are impurities on the surface of samples and Fourier-transform infrared spectroscopy (FTIR) and X-ray photoelectron spectroscopy (XPS) confirmed that the chemical composition of the impurity is mainly Li_2CO_3. The XPS results verified that the generation of a Li_2CO_3 layer together with a NiO rock-salt structure is the obstacle for the delithiation reaction of bulk NCM and seriously damages the electrochemical performance. Finally, the domain of the high nickel cathode material was observed by transmission electron microscopy (TEM) to reveal the difference in the rate and cycling properties of single crystal and polycrystalline cathodes. Through the comparison of different aging behaviors of P-NCM811 and S-NCM811, the design route of Ni-rich cathode materials is proposed to reach better performance.

2.   Results and discussion

The microstructure of P-NCM811 consists of spherical secondary particles (Fig. 1a) formed by the agglomeration of primary nanoparticles with a median particle size of 17.2 μm (inset in Fig. 1a). Fig. S1a† shows an enlarged view of the

particle surface agglomerates with small crystals of ∼1 μm. S-NCM811 has a particle size of 2–5 μm (Fig. 1b) with a median particle size of 3.8 μm. Different particle sizes will affect the performance of the Ni-rich cathode material since a smaller size could decrease the diffusion length of Li^+ in the active materials[33,34] and a bigger size could cause micro-crack and strain formation during intercalation and de-intercalation.[35] For example, on the one hand, Jiang *et al.* showed that with the increase of the $LiCoO_2$ particle size from 0.8 to 2, and then to 5 μm, the thermal stability of $Li_{0.5}CoO_2$ was greatly improved.[33] On the other hand, Zhang *et al.* indicated that NCM811 cathode powder with D_{50} = 7.7 μm displayed the best electrochemical performance by comparing NCM811 with a D_{50} of 3.8, 4.1, 5.5, 7.7 and 8.6 μm, respectively.[34] In addition, Strauss *et al.* showed the benefits of using small particles ($d \leq 10$ μm), allowing virtually full charge capacity in all-solid-state batteries.[35] Therefore, selecting an appropriate particle size is an important factor for improving the structural stability and electrochemical performance of active materials for LIBs. Fig. 1c shows the XRD patterns of P-NCM811 and S-NCM811 samples at room temperature, and it was observed that all the diffraction peaks were clear and sharp, which indicated that the samples were well crystallized.[36] Both samples were indexed to the layered α-$NaFeO_2$ structure with an $R3m$ space group.[27] Rietveld refinements of XRD patterns with the lattice parameters are listed in Table S1.† The lattice constants a and c of P-NCM811 are a = 2.874 Å and c = 14.208 Å, but those values of S-NCM811 change to a = 2.884 Å and c = 14.246 Å, respectively. Especially, the c value of S-NCM811 is larger than that of P-NCM811 because of smaller Ni^{3+} (Table S1†). Generally, the intensity ratio of (003) to (104) peak ($I(003)/I(104)$) is indicative of the degree of cation mixing in the layered structure with an $R3m$ space group. Ni^{2+} ions (0.69 Å) which have a similar ionic radius to Li^+ (0.76 Å) tend to migrate to Li slabs.[37] The high value of $I(003)/I(104)$ and c/a (>4.899) indicated good cation ordering and a layered structure, respectively.[10] Fig. S2† displays the chemical composition of NCM, analyzed by using inductively coupled plasma optical emission spectroscopy (ICP-OES) (detailed value in Table S2†), which gives the total amount of each element regardless of its spatial distribution and phase. The proportion of Ni : Co : Mn is close to 8 : 1 : 1 for both P-NCM811 and S-NCM811. These two samples were heated to different temperatures to explore the difference in thermal stability between single-crystal and polycrystalline Ni-rich cathode materials. Fig. 1d shows that the volume change rate of P-NCM811 is larger than that of S-NCM811 with the increase of temperature. The thermogravimetric (TG) analysis of P-NCM811 and S-NCM811 is shown in Fig. S3,† which further verified that S-NCM811 has better temperature stability than P-NCM811. To improve the structural stability and electrochemical performance of polycrystalline Ni-rich cathodes, a method must be developed to dissipate the internal stress caused by the detrimental phase transition due to heat[38] or electrochemistry.[6,12] As shown in Fig. 1e, one proposed method is to control the primary particle orientations to form a uniform geometry, such as petal-like single-crystal aggregation into secondary particles as a potential scheme to improve thermal stability so that the primary
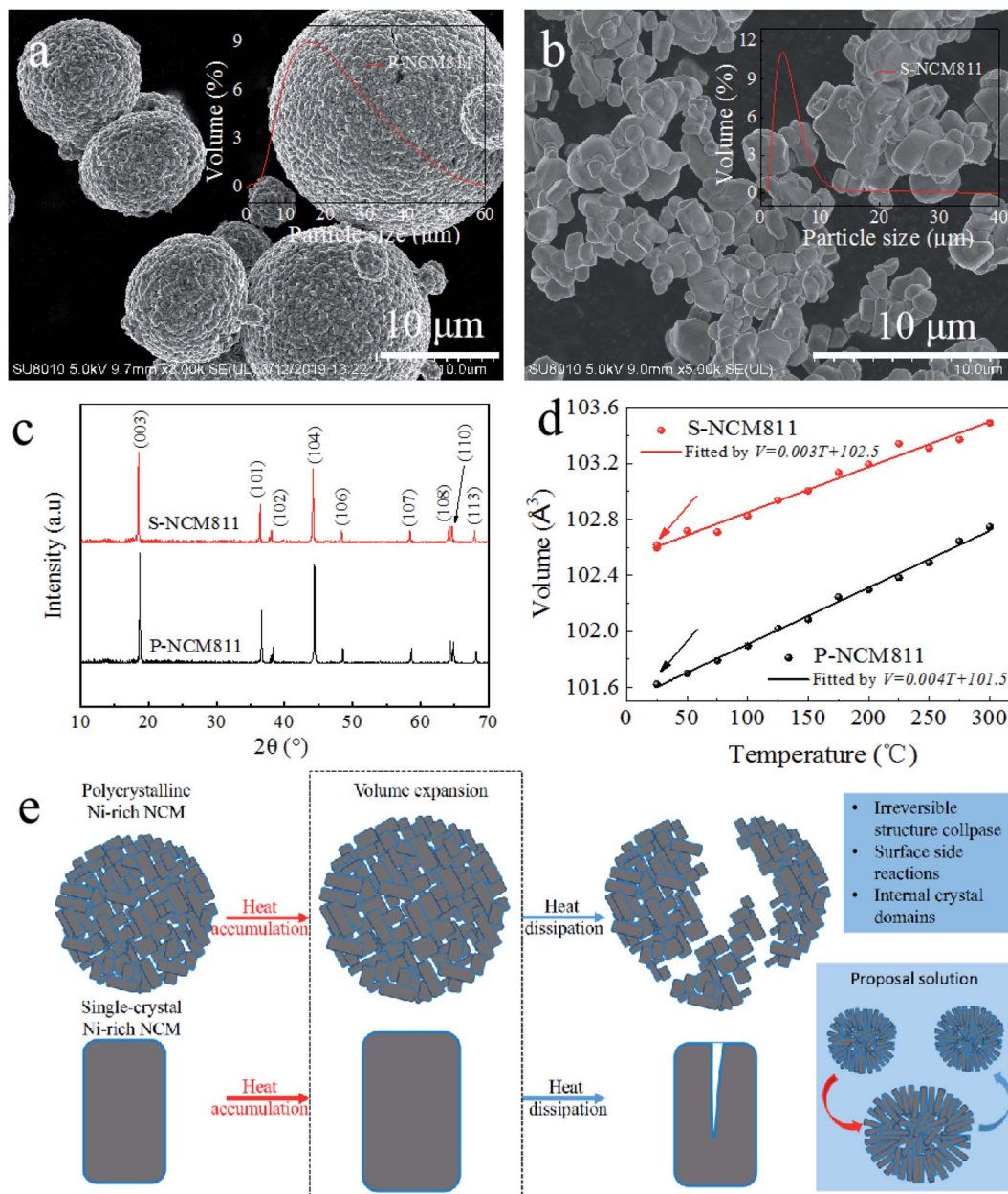
Fig. 1 SEM images of (a) P-NCM811 and (b) S-NCM811. (c) XRD patterns. (d) Volume change. (e) Scheme of thermal aggregation failure comparison between single-crystal and polycrystalline Ni-rich cathode materials and proposed solution.

particles contract and expand uniformly rather than in a random direction.

The NCM systems with a progressively higher nickel content from NCM 111, 532, 622, to 811 follow a steady trend in decreased cycling stability and safety.[7,39] Similarly, the structural stability of NCM materials will also decrease with the increase of nickel content; especially when the battery works, it will give off heat, which has a great influence on the structure of Ni-rich cathode materials.[10,40] Therefore, *ex situ* SEM was employed to observe the structural changes of P-NCM811 and S-NCM811 after heat treatment at room temperature, 100, 200 and 300 °C, which are shown in Fig. S4.† As the temperature increases, the cracks of P-NCM811 increase, and the irreversible

morphological changes become more obvious (Fig. S4a2 and S4a3†), and the secondary particles break into hemispherical particles (Fig. S4b2†) or even smaller particles (Fig. S4b3†). However, for S-NCM811, with the increment of temperature, single crystal particles only have some cracks without complete rupture, as shown in Fig. S4d1 and S4d2.† The broader and consistent cracks of P-NCM811 are summarized in Fig. S5.† Hence, it can be seen from the *ex situ* SEM results that the temperature resistance of single crystal particles is better than that of polycrystalline particles. As reported in the literature, local stress concentrations are produced in micro-cracks along the inter-particle boundaries.[41] Micro-cracks allow the infiltration of electrolytes into the interior of the secondary particles

19682 | *J. Mater. Chem. A*, 2022, **10**, 19680–19689

This journal is © The Royal Society of Chemistry 2022

and expose the internal surfaces to be attacked by the electrolytes.[42] These micro-cracks undermine the mechanical integrity of the cathode particles in addition to the loss of electrochemical activity from the parasitic reactions at the cathode–electrolyte interfaces.[43] Thus, suppressing the micro-cracking is key to alleviate the rapid capacity fading of Ni-rich layered cathodes. Removing the inter-particle boundaries by developing single-crystalline cathodes has emerged as a promising strategy.[44] Single-crystalline cathodes, free from inter-particle micro-cracking, are shown to improve cycling and thermal stability by minimizing parasitic surface degradation.

In situ XRD was employed to further investigate the structural stability difference, especially, the phase and volume changes in the crystal structure of P-NCM811 and S-NCM811 during the heating process (Fig. 2). The two samples were heated from room temperature (25 °C) to 300 °C, measuring them every 25 °C, and finally measuring again after dropping to room temperature to observe the irreversible crystal phase and volume changes. When scanning every 25 °C, the peak position is always shifted to the left as shown in Fig. 2a and b. An expansion along the *c* axis is expected from the shift of (003) to a lower angle, also seen from Table S3.† The *c* value of P-NCM811 at the initial state is 14.208 Å, which increases to 14.281 Å at 300 °C. When the temperature drops to room temperature, the *c* value is 14.219 Å. However, for S-NCM811, the *c* value is consistent with that in the initial state after the same heat treatment process. This is because the increasing temperature led to an increased repulsion force between two neighboring TM-O slabs and an increased lattice parameter along the *c* axis resulting in a decreased in 2θ of the (003) peak. It is exceptionally comparable to the delithiation process during charging.[41] In Fig. 2c, the different axial and volume changes after heat treatment of P-NCM811 were stronger than those of S-NCM811, which demonstrated that the phase transition of polycrystalline materials with temperature increase is more intense than that of single crystal materials. As shown in Fig. 2d, the phase change of a single crystal is drastic, but the recovery is better. Herein, both *ex situ* SEM and *in situ* XRD results show that single crystal materials have better structural stability.

Because of the different structural stability, P-NCM811 shows quite different electrochemical performance compared with S-NCM811. The NCM/lithium half cells were first cycled at 0.2C rate for three cycles of activation and then cycled at 1C rate between 2.8 V and 4.3 V. The initial charge–discharge profiles at 0.2C rate of P-NCM811 is 174.4 mA h g^{-1} and 138.2 mA h g^{-1} in the 10th cycle (1C rate). Meanwhile, the initial charge–discharge profiles at 0.2C rate of S-NCM811 is 197.9 mA h g^{-1} and 161.8 mA h g^{-1} in the 10th cycle (1C rate), as shown in Fig. 3a and 3b. The rate performance of S-NCM811 is much better than that of P-NCM811 from 0.2C to 2C rate (Fig. 3c). Similarly, the capacity of S-NCM faded slowly after 200 cycles at 1C rate with a capacity retention of 79.7%. In contrast, the capacity retention of P-NCM811 after 200 cycles at 1C is only 72.1%. The rapid capacity fading of P-NCM811 cathodes is largely caused by the side reactions at the formed micro cracks and electrolyte interface, resulting in the buildup of NiO-like rock salt phases.[6,9] In contrast, owing to the fast lithium-ion pathways and stable

structure of S-NCM811, the electrochemical results show that the single-crystal material not only has a higher specific capacity but also has better rate performance and cycle stability.

In order to find out the impact of the surface state on the electrochemical performance, cyclic voltammetry (CV) characterization was performed for the first three cycles and after 200 cycles at a scan rate of 0.05 mV s^{-1} with an upper cut off voltage of 4.5 V. In Fig. 3e and f, three pairs of redox peaks are observed from 2.8 to 4.5 V corresponding to the different phase transformations, as reported in other literature.[6,45] The original layered structure (H1) transitioned to a monoclinic phase (M) at ~3.75 V, M-H2 transitioned at ~4.0 V and H2–H3 transitioned at ~4.2 V, where H2 and H3 are two hexagonal phases. Notably, a common feature that is easily observed for CV data is the evident difference between the initial delithiation peak (purple line) and that upon the following cycles. There is an activation process comparing the first and the following cycles in the CV of P-NCM as shown in Fig. 3a. The activation potential is 3.84 V for P-NCM811 and there is less obvious activation behavior in S-NCM (Fig. 3b). The activation potential should be mainly caused by the surface impurity film (the bulk structure rearrangement of the Li$_2$CO$_3$ surface film).[37,46,47] The impurity surface film serves as a barrier for the lithium (de)insertion reaction's kinetics.[12] The P-NCM811 sample with a more surface impurity layer displays a much more obvious activation process. However, after cycling for 200 cycles, both P-NCM811 (Fig. S6a†) and S-NCM811 (Fig. S6b†) have no obvious activation behavior. The peak potential shifts towards the left with cycling, which suggests that the degradation reaction of Li$_2$CO$_3$ occurs during the subsequent cycling.[48] The cycling stability of a single crystal is better than that of the polycrystalline cathode material from the CV curves after 200 cycles because the CV changes in P-NCM811 (Fig. S5a†) is significantly faster than that from S-NCM811 (Fig. S5b†), which is also consistent with the cycling results (Fig. 3d).

The chemical states of the surface elements were also investigated by X-ray photoelectron spectroscopy (XPS). The main elements are displayed in Fig. 4a, with their fine sections shown in Fig. 4b–f. The surface of the two samples is dominated by C and O. To get a better understanding of the surface chemistry, the C 1s and O1s spectra are analyzed with MultiPak software as shown in Fig. 4b and c. The C 1s spectra can be divided into three peaks corresponding to CO$_3^{2-}$ (289.8 eV), C=O (286.5 eV), and C–C (284.8 eV). The area proportion of the peak at 289.8 eV (CO$_3^{2-}$) is 17.8% and 9.4% for P-NCM811 and S-NCM811, respectively. The O 1s spectra can be fitted with two peaks, indexed to O$_{impurity}$ (531.9 eV) and O$_{lattice}$ (529.5 eV). The O$_{impurity}$ is mainly originated from the active oxygen species O$^-$, O^{2-}, or CO$_3^{2-}$ of the Li$_2$CO$_3$ impurity layer. The O$_{lattice}$ is derived from the lattice oxygen O^{2-} of the M–O (M = Ni, Co, Mn) bond. Note that the area percentage of O$_{lattice}$ is 2.8% for P-NCM811 and 43.2% for S-NCM811. It infers that the surface of P-NCM811 is covered by an impurity layer, mainly composed of Li$_2$CO$_3$. This is inconsistent with the weak signals of transition metal elements in Fig. 4d–f. The peaks of Ni 2p (873 and 855 eV), Co 2p (796 and 780 eV), and Mn 2p (654 and 643 eV) can be seen S-NCM811, but they are not apparent in P-NCM811. The
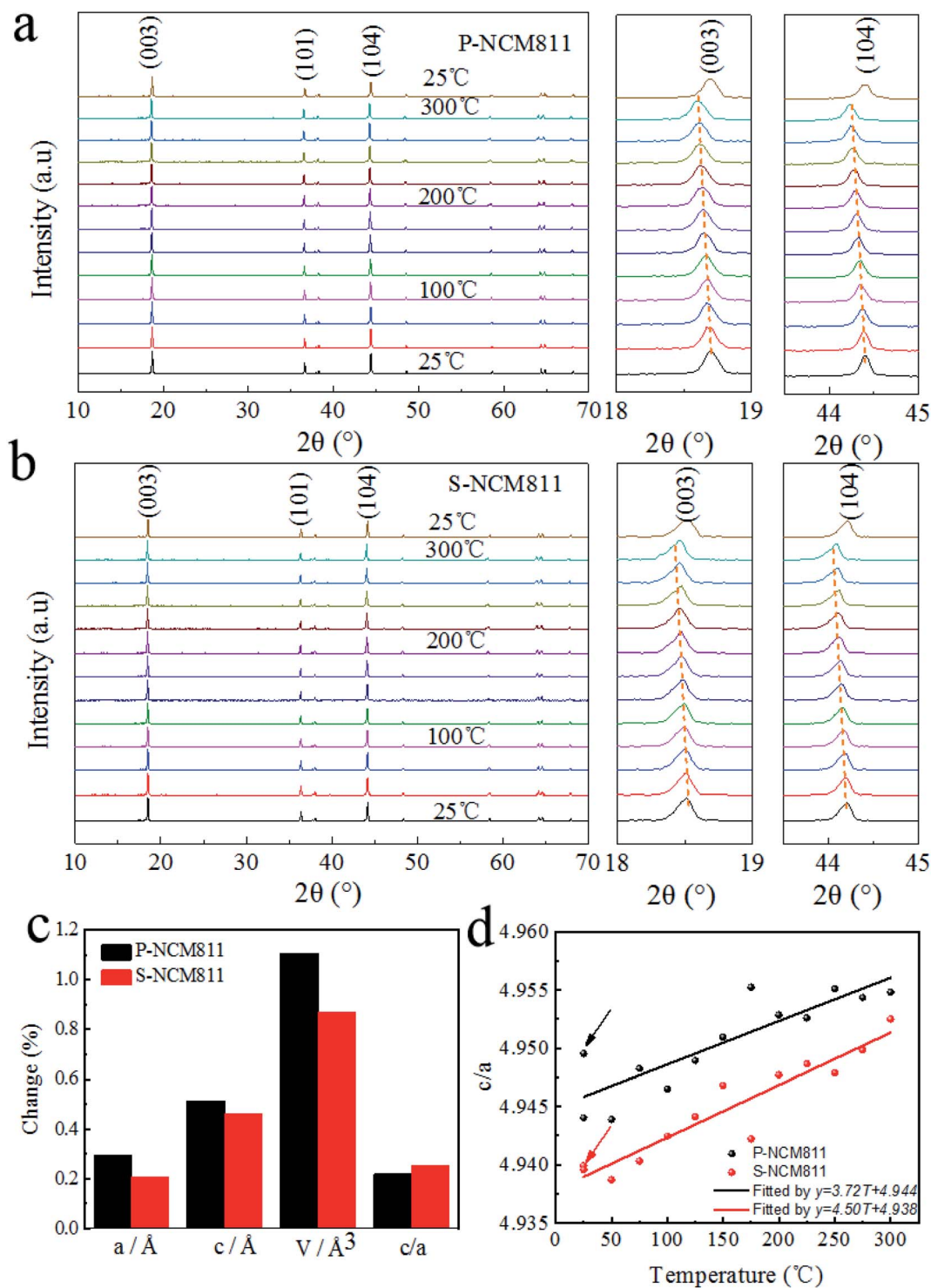
This journal is © The Royal Society of Chemistry 2022

J. Mater. Chem. A, 2022, **10**, 19680–19689 | **19683**

Fig. 2 *In situ* XRD of (a) P-NCM811 and (b) S-NCM811 cathode materials. Detailed 2θ degree ranges of 18.0–19.0° and 43.5–45° are also displayed. (c) Lattice and volume change. (d) The change of c/a with the increasement of the temperature.

reduced signal is mainly caused by the thick impurity layer on the surface.[49]

Fourier transform infrared spectroscopy (FT-IR) was applied to investigate the surface chemical composition of the two samples as shown in Fig. S7.† The peak at 530 cm^{-1} represents the metal–oxygen bond (M–O, M = Ni, Co, Mn), which is

observed in the two samples. The peaks at 1488 and 1438 cm^{-1} are caused by the antisymmetric stretching vibration of the –CO$_3$ group and the peak at 868 cm^{-1} is due to the out-of-plane bending vibration of the –CO$_3$ group. These peak signals indicate that the impurities are composed of carbonate. Furthermore, it has been recognized that these surface impurities are
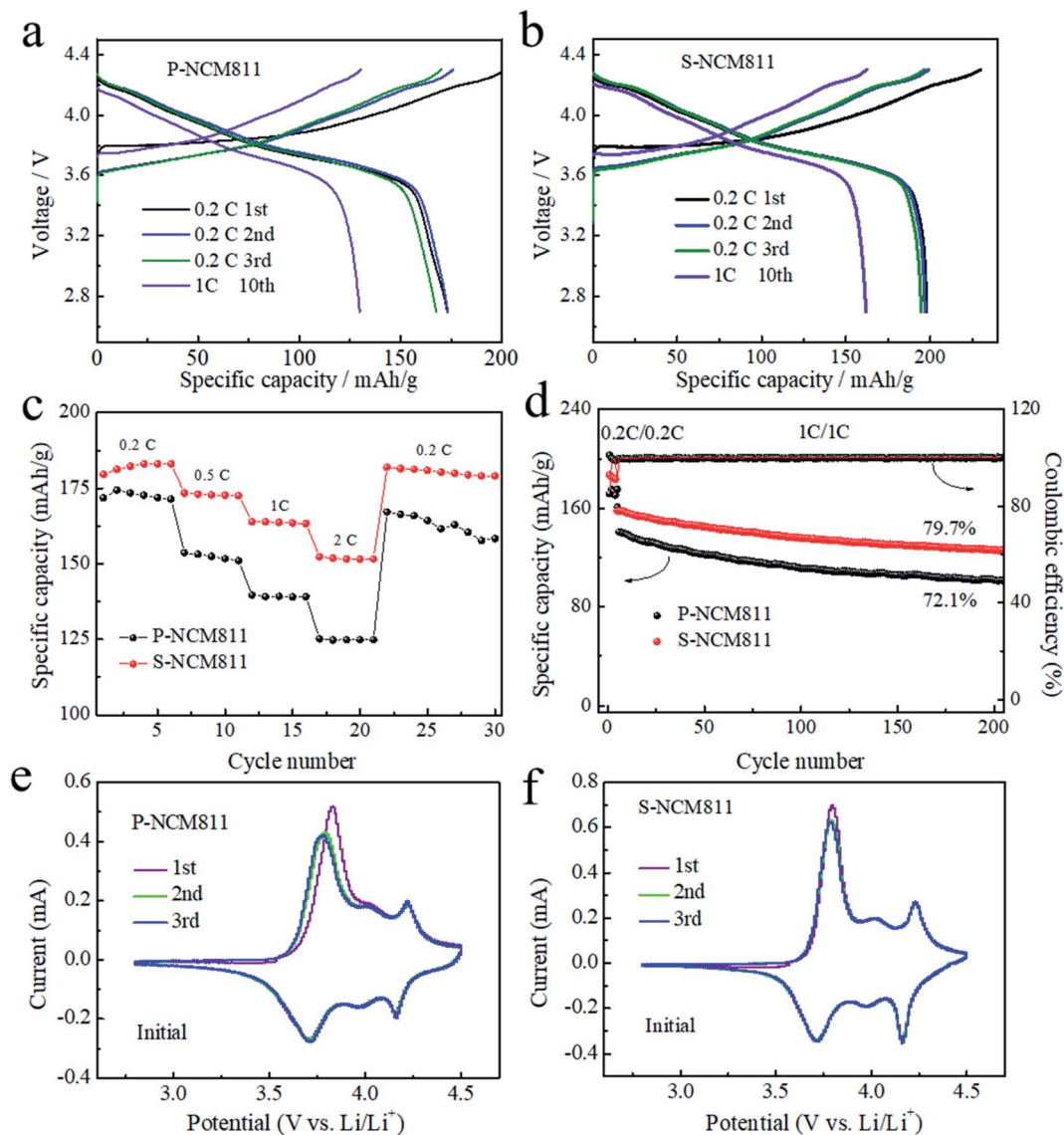
19684 | *J. Mater. Chem. A*, 2022, **10**, 19680–19689

This journal is © The Royal Society of Chemistry 2022

Fig. 3 The charge–discharge curves of (a) P-NCM811 and (b) S-NCM811. (c) Rate and (d) cycling performance. Cyclic voltammetry characterization of (e) P-NCM811 and (f) S-NCM811 at the initial state.

electrochemically inactive due to their poor electronic conductivity and low lithium ion conductivity.[50] Therefore, reducing the amounts of lithium residual impurities is very important because they block the channels for Li-ion transportation. In our previous study, we addressed the failure and recovery behaviors of stored Ni-rich NCMs, and proposed a simple and effective method to remove these barriers using high-temperature calcination with an oxygen flow (*e.g.*, 800 °C for 3 h).[51] During this process, the lithium ions in the Li_2CO_3 layer can return to the lattice, and the rock-salt phase can be transformed back to the original layered structure with the oxidation of Ni^{2+} and Ni^{3+}.

To better see the lattice structure of single crystal and polycrystalline materials, detailed structures near the surface region are clarified in the high-resolution TEM images. We used Cyro-Focused Ion Beam Scanning Electron Microscopy (FIB-SEM) to

prepare samples. The detailed process is shown in Fig. S8† to obtain fragment samples. Fig. 5 displays the high resolution TEM and fast Fourier transformed (FFT) images of P-NCM811 and S-NCM811. As shown in Fig. 5a, the surface region of P-NCM811 forms an impurity later consisting of a mixed phase of the NiO phase and Li_2CO_3 film. The Li_2CO_3 layer is formed by the interaction between the active Li^+ in the near-surface lattice and H_2O/CO_2 in air, which is in agreement with the CV, XPS and FTIR results. During this process, Ni^{3+} can spontaneously reduce to Ni^{2+} to produce the NiO rock-salt structure. The thick Li_2CO_3 layer and the inactive NiO phase will become dual barriers to the kinetics of bulk NCM materials. In Fig. 5b, there are crystal domains in polycrystalline materials and the lattice gaps on both sides are different, which directly leads to poor ion mobility. The results are also in good agreement with the measured values in ref. 32 and 51. Fig. 5c and d show more
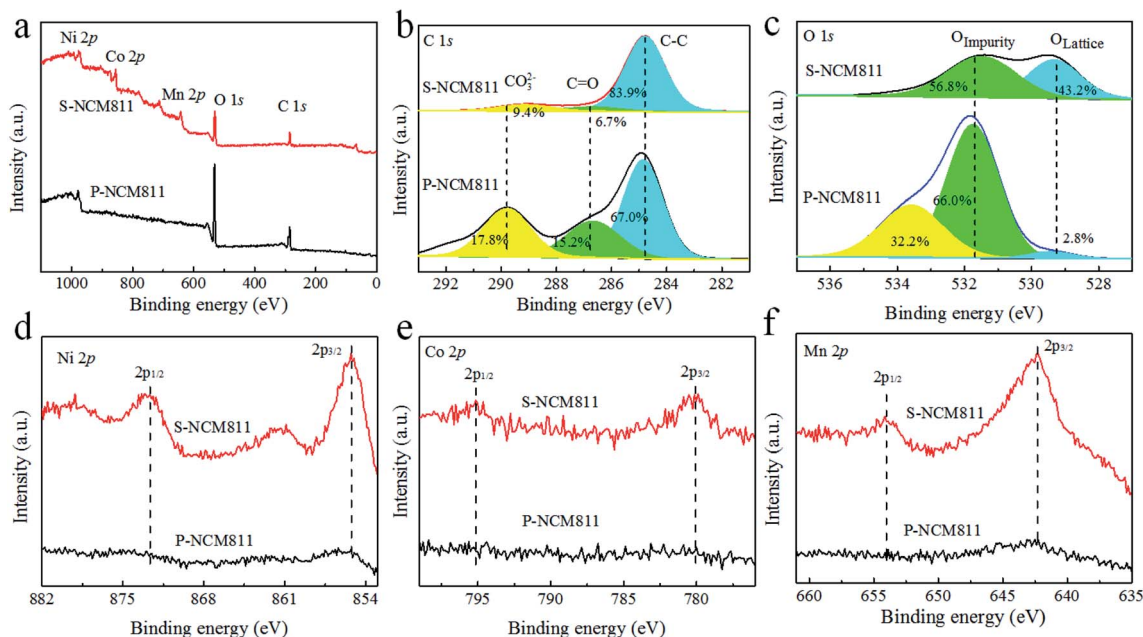
Fig. 4 Surface elements of S-NCM811 and P-NCM811 determined through XPS analysis (a). XPS spectra of (b) C 1s, (c) O 1s, (d) Ni 2p, (e) Co 2p and (f) Mn 2p.

crystal domains found in P-NCM811. However, S-NCM811 only demonstrated the rhombohedral phase (Fig. 5e). The TEM analysis also strongly suggests that P-NCM811 is more likely to have a disordered inner and surface structure, resulting in worse cycling stability and rate performance. In addition, high-resolution TEM revealed that a NiO rock-salt structure was formed in the near-surface region of P-NCM811. The Li_2CO_3 layer together with the NiO rock-salt structure is the obstacle for the delithiation reaction of bulk NCM and seriously damages the electrochemical performance.
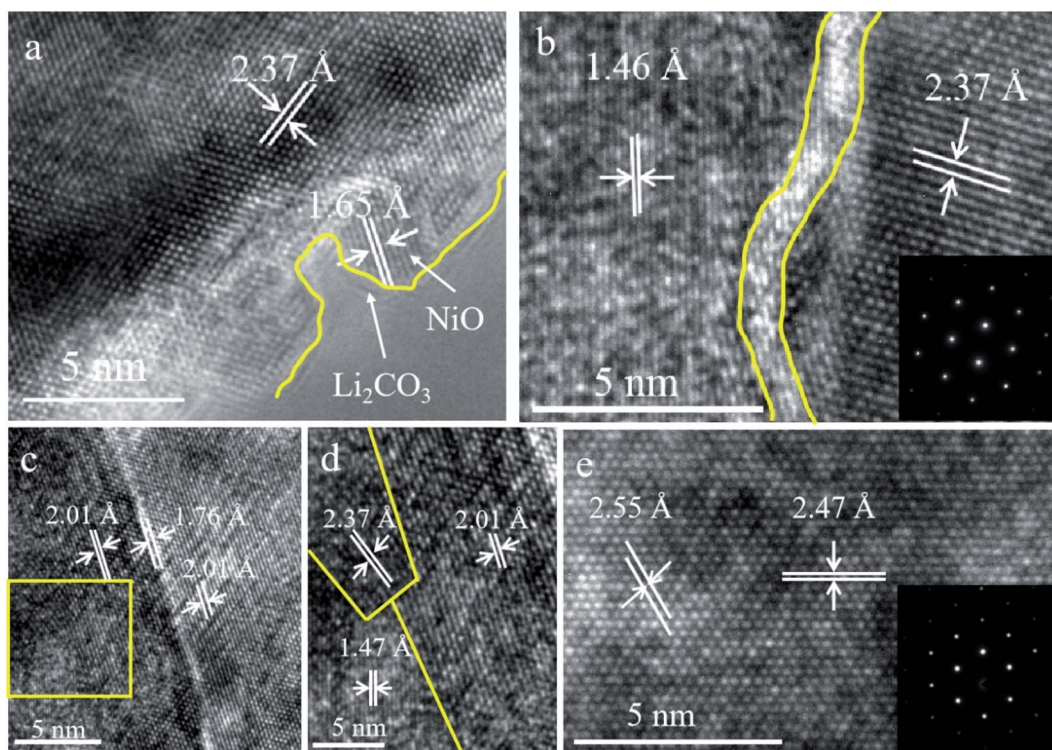

Fig. 5 HR-TEM and FFT images of P-NCM811 (a–d) and S-NCM811(e).

3. Conclusion

In summary, the aging behaviors of Ni-rich cathode materials were carefully investigated by comparing P-NCM811 and S-NCM811. Firstly, *in situ* XRD and *ex situ* SEM show that polycrystalline materials have higher irreversible properties than single crystals with the increase of temperature, resulting in poor cycling and rate properties. In addition, CV results shows that there are impurities on the surface of samples and FTIR, XPS, and TEM confirmed that the chemical composition of the impurity is mainly Li_2CO_3. The XPS results verified that the generation of the Li_2CO_3 layer together with a NiO rock-salt structure is the obstacle for the delithiation reaction of bulk NCM and seriously damages the electrochemical performance. Furthermore, high-resolution TEM revealed that the NiO rock-salt structure was formed in the near-surface region. And the TEM results also show that there are many crystal domains in the polycrystalline high nickel positive electrode, which will prevent the rate performance. Surface side reaction and internal crystal domains that produce structural defects were discovered to impair lithium ion diffusion and, as a result, lead to rapid capacity fading and poor cycling stability. Looking forward, from the perspective of material design, we need to combine the advantages of polycrystalline and single-crystal materials to achieve safer and higher energy density Ni-rich cathode materials.

4. Experimental section

4.1 Preparation of cathode materials

The commercial Ni-rich $LiNi_{0.8}Co_{0.1}Mn_{0.1}O_2$ was supplied by Hunan Changyuan Lico Co. Ltd (China).

4.2 characterization

The morphologies of particles were observed by using a SEM SU8010 (Hitachi Corporation, Japan). The crystal structure was characterized by using XRD with a Bruker D8 Advance diffractometer (Bruker, Billerica, MA), which operated at 40 kV and 40 mA with Cu Kα radiation at a scan rate of $5° \text{ min}^{-1}$ from $10°$–$90°$. XPS was performed on a PHI 5000 Versaprobe II (Ulvac-Phi, Japan) using an Al Kα (1486.6 eV) excitation source, and the binding energy was corrected with C 1s (284.8 eV) as a reference. TEM was performed on a Tecnai G2 F30 (FEI, Hillsboro OR) to record the microstructure and surface lattice images. ICP-OES was carried out on an ARCOS II MV (Spectro, Germany) to distinguish the chemical composition of the two samples. FT-IR was performed by using a Nicolet iS 50 (Thermo Fisher Scientific, Waltham, MA) with the pellet method over the range of 400–4000 cm^{-1}. The particle size distribution was measured by using a Mastersizer 2000Hydro 2000MU (Malvern, England) with an ultrasonic frequency of 50 Hz and utilizing deionized water as a dispersing agent.

4.3 Electrochemical measurements

The electrochemical performance was tested in coin-type cells (CR2032). The NCM powder was mixed with carbon black and polyvinylidene fluoride (PVDF) in a weight ratio of 8 : 1 : 1 in *N*-methyl-1,2-pyrrolidone (NMP) solvent. The slurry was spread onto Al foil by utilizing the doctor blade method and dried in a vacuum oven at 110 °C overnight, and then punched into discs of 12 mm diameter. The active material loading level was controlled to be $\sim3 \text{ mg cm}^{-2}$. The CR2032 coin-type cells were assembled with the cathode, a Li metal anode, a separator (Celgrad 2400), and an organic electrolyte (1 M $LiPF_6$, EC/DMC/FEC 1 : 1 : 1 vol%) in an argon-filled glovebox (LABstar MBRAUN, Germany). The cycling and rate performances from 0.2C to 2C (1C = 170 mA h g^{-1}) were assessed on a battery testing system (LAND CT 2001A, China) between 2.8 and 4.3 V at 25 °C. Cyclic voltammetry (CV) was performed on a VMP3 system (Bio-Logic, France) with a scan rate of 0.05 mV s^{-1} in a voltage window of 2.8–4.5 V.

Author contributions

A. H. Ran, X. Zhang and G. D. Wei conceived this study. A. H. Ran and S. X. Chen carried out experiments. A. H. Ran, M. Cheng, and Z. Liang analyzed the data. B. H. Li, G. M. Zhou and F. Y. Kang discussed this work. A. H. Ran wrote this paper. G. M. Zhou, X. Zhang and G. D. Wei revised this paper.

Conflicts of interest

The authors declare that they have no conflict of interest.

Acknowledgements

References

1 P. Albertus, J. S. Manser and S. Litzelman, Long-Duration Electricity Storage Applications, Economics, and Technologies, *Joule*, 2020, **4**, 21–32.

2 M. Lewerenz, A. Marongiu, A. Warnecke and D. U. Sauer, Differential voltage analysis as a tool for analyzing inhomogeneous aging: A case study for $LiFePO_4$|Graphite cylindrical cells, *J. Power Sources*, 2017, **368**, 57–67.

3 B. W. Xiao and X. L. Sun, Surface and Subsurface Reactions of Lithium Transition Metal Oxide Cathode Materials: An Overview of the Fundamental Origins and Remedying Approaches, *Adv. Energy Mater.*, 2018, **8**, 1802057.

4 N. Yabuuchi, K. Yoshii, S. T. Myung, I. Nakai and S. Komaba, Detailed studies of a high-capacity electrode material for rechargeable batteries, Li_2MnO_3–$LiCo_{(1/3)}Ni_{(1/3)}Mn(1/3)O_2$, *J. Am. Chem. Soc.*, 2011, **133**, 4404–4419.

5 C. S. Yoon, *et al.*, High-Energy Ni-Rich $Li[Ni_xCo_yMn_{1-x-y}]O_2$ Cathodes *via* Compositional Partitioning for Next-

This journal is © The Royal Society of Chemistry 2022

J. Mater. Chem. A, 2022, **10**, 19680–19689 | **19687**

Generation Electric Vehicles, *Chem. Mater.*, 2017, **29**, 10436–10445.

6 H.-H. Ryu, K.-J. Park, C. S. Yoon and Y.-K. Sun, Capacity Fading of Ni-Rich Li[NixCoyMn$_{1-x-y}$]O$_2$ (0.6 ≤ x ≤ 0.95) Cathodes for High-Energy-Density Lithium-Ion Batteries: Bulk or Surface Degradation?, *Chem. Mater.*, 2018, **30**, 1155–1163.

7 S. T. Myung, *et al.*, Nickel-Rich Layered Cathode Materials for Automotive Lithium-Ion Batteries: Achievements and Perspectives, *ACS Energy Lett.*, 2017, **2**, 196–223.

8 Y. K. Sun, *et al.*, Nanostructured high-energy cathode materials for advanced lithium batteries, *Nat. Mater.*, 2012, **11**, 942–947.

9 H. Liu, *et al.*, Intergranular Cracking as a Major Cause of Long-Term Capacity Fading of Layered Cathodes, *Nano Lett.*, 2017, **17**, 3452–3457.

10 G. Sun, *et al.*, The effect of cation mixing controlled by thermal treatment duration on the electrochemical stability of lithium transition-metal oxides, *Phys. Chem. Chem. Phys.*, 2017, **19**, 29886–29894.

11 M. Song and S.-Y. Choe, Fast and safe charging method suppressing side reaction and lithium deposition reaction in lithium ion battery, *J. Power Sources*, 2019, **436**, 226835.

12 L. Li, *et al.*, Alleviating Surface Degradation of Nickel-Rich Layered Oxide Cathode Material by Encapsulating with Nanoscale Li-Ions/Electrons Superionic Conductors Hybrid Membrane for Advanced Li-Ion Batteries, *ACS Appl. Mater. Interfaces*, 2016, **8**, 30879–30889.

13 Y. You, H. Celio, J. Li, A. Dolocan and A. Manthiram, Modified High-Nickel Cathodes with Stable Surface Chemistry Against Ambient Air for Lithium-Ion Batteries, *Angew. Chem., Int. Ed. Engl.*, 2018, **57**, 6480–6485.

14 S. E. Renfrew and B. D. McCloskey, Residual Lithium Carbonate Predominantly Accounts for First Cycle CO2 and CO Outgassing of Li-Stoichiometric and Li-Rich Layered Transition-Metal Oxides, *J. Am. Chem. Soc.*, 2017, **139**, 17853–17860.

15 H. Zhang, *et al.*, Facet-Dependent Rock-Salt Reconstruction on the Surface of Layered Oxide Cathodes, *Chem. Mater.*, 2018, **30**, 692–699.

16 J. H. Kim, H. H. Ryu, S. J. Kim, C. S. Yoon and Y. K. Sun, Degradation Mechanism of Highly Ni-Rich Li[NixCoyMn$_{1-x-y}$]O$_2$ Cathodes with x > 0.9, *ACS Appl. Mater. Interfaces*, 2019, **11**, 30936–30942.

17 G. N. Qian, *et al.*, Single-crystal nickel-rich layered-oxide battery cathode materials: synthesis, electrochemistry, and intra-granular fracture, *Energy Storage Mater.*, 2020, **27**, 140–149.

18 Y. Zhao, *et al.*, Surface Structural Transition Induced by Gradient Polyanion-Doping in Li-Rich Layered Oxides: Implications for Enhanced Electrochemical Performance, *Adv. Funct. Mater.*, 2016, **26**, 4760–4767.

19 B. Qiu, *et al.*, Enhanced electrochemical performance with surface coating by reactive magnetron sputtering on lithium-rich layered oxide electrodes, *ACS Appl. Mater. Interfaces*, 2014, **6**, 9185–9193.

20 Y. Li, *et al.*, Stable surface construction of the Ni-rich LiNi$_{0.8}$Mn$_{0.1}$Co$_{0.1}$O$_2$ cathode material for high performance lithium-ion batteries, *J. Mater. Chem. A*, 2020, **8**, 21649–21660.

21 S. Choudhury, *et al.*, Stabilizing polymer electrolytes in high-voltage lithium batteries, *Nat. Commun.*, 2019, **10**, 3091.

22 M. Dong, *et al.*, Metallurgy Inspired Formation of Homogeneous Al$_2$O$_3$ Coating Layer To Improve the Electrochemical Properties of LiNi$_{0.8}$Co$_{0.1}$Mn$_{0.1}$O$_2$ Cathode Material, *ACS Sustainable Chem. Eng.*, 2017, **5**, 10199–10205.

23 X. Xiong, *et al.*, Washing effects on electrochemical performance and storage characteristics of LiNi$_{0.8}$Co$_{0.1}$Mn$_{0.1}$O$_2$ as cathode material for lithium-ion batteries, *J. Power Sources*, 2013, **222**, 318–325.

24 Y. K. Sun, *et al.*, High-energy cathode material for long-life and safe lithium batteries, *Nat. Mater.*, 2009, **8**, 320–324.

25 E. Sahraei, M. Kahn, J. Meier and T. Wierzbicki, Modelling of cracks developed in lithium-ion cells under mechanical loading, *RSC Adv.*, 2015, **5**, 80369–80380.

26 R. Zhang, *et al.*, A Study on the Open Circuit Voltage and State of Charge Characterization of High Capacity Lithium-Ion Battery Under Different Temperature, *Energies*, 2018, **11**, 2408.

27 Z. Feng, *et al.*, Dual-Element-Modified Single-Crystal LiNi$_{0.6}$Co$_{0.2}$Mn$_{0.2}$O$_2$ as a Highly Stable Cathode for Lithium-Ion Batteries, *ACS Appl. Mater. Interfaces*, 2021, **13**, 43039–43050.

28 Y. Sun, *et al.*, Correlation between thermal stabilities of nickel-rich cathode materials and battery thermal runaway, *Int. J. Energy Res.*, 2021, **45**, 20867–20877.

29 H.-J. Noh, *et al.*, Cathode Material with Nanorod Structure— An Application for Advanced High-Energy and Safe Lithium Batteries, *Chem. Mater.*, 2013, **25**, 2109–2115.

30 Y. Sun, *et al.*, Influence of Ni/Mn distributions on the structure and electrochemical properties of Ni-rich cathode materials, *Dalton Trans.*, 2018, **47**, 16651–16659.

31 Z. Zhang, *et al.*, A low cost single-crystalline LiNi$_{0.60}$Co$_{0.10}$Mn$_{0.30}$O$_2$ layered cathode enables remarkable cycling performance of lithium-ion batteries at elevated temperature, *J. Power Sources*, 2021, **503**, 230028.

32 H. H. Ryu, *et al.*, Capacity fading mechanisms in ni-rich single-crystal NCM cathodes, *ACS Energy Lett.*, 2021, **6**, 2726–2734.

33 J. Jiang and J. R. Dahn, Effects of particle size and electrolyte salt on the thermal stability of Li$_{0.5}$CoO$_2$, *Electrochim. Acta*, 2004, **49**, 2661–2666.

34 M. Zhang, *et al.*, Effect of micron sized particle on the electrochemical properties of nickel-rich LiNi$_{0.8}$Co$_{0.1}$Mn$_{0.1}$O$_2$ cathode materials, *Ceram. Int.*, 2020, **46**, 4643–4651.

35 F. Strauss, *et al.*, Impact of cathode material particle size on the capacity of bulk-type all-solid-state batteries, *ACS Energy Lett.*, 2018, **3**, 992–996.

36 Y. Li, *et al.*, Synthesis of full concentration gradient cathode studied by high energy X-ray diffraction, *Nano Energy*, 2016, **19**, 522–531.

19688 | *J. Mater. Chem. A*, 2022, **10**, 19680–19689

This journal is © The Royal Society of Chemistry 2022

37 M. D. Radin, J. Alvarado, Y. S. Meng and A. Van der Ven, Role of Crystal Symmetry in the Reversibility of Stacking-Sequence Changes in Layered Intercalation Electrodes, *Nano Lett.*, 2017, **17**, 7789–7795.

38 R. Genieser, *et al.*, Lithium ion batteries (NMC/graphite) cycling at 80 °C: Different electrolytes and related degradation mechanism, *J. Power Sources*, 2018, **373**, 172–183.

39 Y. Cho, P. Oh and J. Cho, A new type of protective surface layer for high-capacity Ni-based cathode materials: nanoscaled surface pillaring layer, *Nano Lett.*, 2013, **13**, 1145–1152.

40 S.-M. Bak, *et al.*, Correlating Structural Changes and Gas Evolution during the Thermal Decomposition of Charged $Li_xNi_{0.8}Co_{0.15}Al_{0.05}O_2$ Cathode Materials, *Chem. Mater.*, 2013, **25**, 337–351.

41 M. Hou, *et al.*, Morphological effect on high compaction density nickel-rich layered oxide cathodes during electrochemical lithiation and delithiation, *Electrochim. Acta*, 2021, **377**, 138118.

42 X. Xu, *et al.*, Radially Oriented Single-Crystal Primary Nanosheets Enable Ultrahigh Rate and Cycling Properties of $LiNi_{0.8}Co_{0.1}Mn_{0.1}O_2$ Cathode Material for Lithium-Ion Batteries, *Adv. Energy Mater.*, 2019, **9**, 1803963.

43 D. J. Miller, C. Proff, J. G. Wen, D. P. Abraham and J. Bareño, Observation of Microstructural Evolution in Li Battery Cathode Oxide Particles by *In Situ* Electron Microscopy, *Adv. Energy Mater.*, 2013, **3**, 1098–1103.

44 J. Zhao, *et al.*, *In Situ* Probing and Synthetic Control of Cationic Ordering in Ni-Rich Layered Oxide Cathodes, *Adv. Energy Mater.*, 2017, **7**, 1601266.

45 H. H. Ryu, G. T. Park, C. S. Yoon and Y. K. Sun, Microstructural Degradation of Ni-Rich $Li[Ni_xCo_yMn_{1-x-y}]O_2$ Cathodes During Accelerated Calendar Aging, *Small*, 2018, **14**, e1803179.

46 W. Li, B. Song and A. Manthiram, High-voltage positive electrode materials for lithium-ion batteries, *Chem. Soc. Rev.*, 2017, **46**, 3006–3059.

47 C. Fang, *et al.*, Quantifying inactive lithium in lithium metal batteries, *Nature*, 2019, **572**, 511–515.

48 K. Qian, *et al.*, Increase and discretization of the energy barrier for individual $LiNi_xCo_yMn_yO_2$ ($x + 2y = 1$) particles with the growth of a Li_2CO_3 surface film, *J. Mater. Chem. A*, 2019, **7**, 12723–12731.

49 K. Park, *et al.*, Metal phosphate-coated Ni-rich layered oxide positive electrode materials for Li-ion batteries: improved electrochemical performance and decreased Li residuals content, *Electrochim. Acta*, 2017, **257**, 217–223.

50 S. Kim, W. Cho, X. Zhang, Y. Oshima and J. W. Choi, A stable lithium-rich surface structure for lithium-rich layered cathode materials, *Nat. Commun.*, 2016, **7**, 13598.

51 B. H. Huang, *et al.*, A Simple Method for the Complete Performance Recovery of Degraded Ni-rich $LiNi_{0.70}Co_{0.15}Mn_{0.15}O_2$ Cathode *via* Surface Reconstruction, *ACS Appl. Mater. Interfaces*, 2019, **11**, 14076–14084.

This journal is © The Royal Society of Chemistry 2022

J. Mater. Chem. A, 2022, **10**, 19680–19689 | **19689**